Journal of Colloid and Interface Science 590 (2021) 199–209

Contents lists available at ScienceDirect

Journal of Colloid and Interface Science

journal homepage: www.elsevier.com/locate/jcis

Regular Article

Topological origin of phase separation in hydrated gels

Cheng Zhao [a,b], Wei Zhou [a,*], Qi Zhou [b], Zhe Wang [b], Gaurav Sant [c,d,e], Lijie Guo [f,*], Mathieu Bauchy [b,e,*]

[a] State Key Laboratory of Water Resources and Hydropower Engineering Science, Wuhan University, Wuhan 430072, China
[b] Physics of AmoRphous and Inorganic Solids Laboratory (PARISlab), Department of Civil and Environmental Engineering, University of California, Los Angeles, CA 90095, USA
[c] Laboratory for the Chemistry of Construction Materials (LC^2), Department of Civil and Environmental Engineering, University of California, Los Angeles, CA 90095, USA
[d] California Nanosystems Institute (CNSI), University of California, Los Angeles, CA 90095, USA
[e] Institute for Carbon Management (ICM), University of California, Los Angeles, CA 90095, USA
[f] National Centre for International Research on Green Metal Mining, BGRIMM Technology Group, Beijing 100160, China

GRAPHICAL ABSTRACT

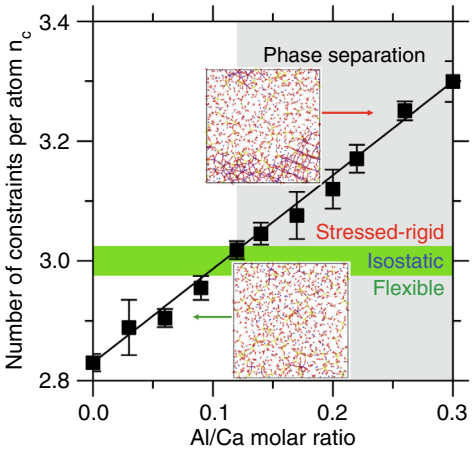

ARTICLE INFO

Article history:
Received 21 September 2020
Revised 20 January 2021
Accepted 21 January 2021
Available online 26 January 2021

Keywords:
Hydrated colloidal gels
Phase separation
Molecular dynamics
Topological constraint theory
Atomic stress

ABSTRACT

Hypothesis: Depending on their composition, hydrated gels can be homogeneous or phase-separated, which, in turn, affects their dynamical and mechanical properties. However, the nature of the structural features, if any, that govern the propensity for a given gel to phase-separate remains largely unknown. Here, we argue that the propensity for hydrated gels to phase-separate is topological in nature.
Simulations: We employ reactive molecular dynamics simulations to model the early-age precipitation of calcium–alumino–silicate–hydrate (C—A—S—H) gels with varying compositions, i.e., $(CaO)_{1.7}(Al_2O_3)_x(SiO_2)_{1-x}(H_2O)_{3.7+x}$. By adopting topological constraint theory, we investigate the structural origin of phase separation in hydrated gels.
Findings: We report the existence of a homogeneous-to-phase-separated transition, wherein Si-rich ($x \leq 0.10$) C—A—S—H gels are homogeneous, whereas Al-rich ($x > 0.10$) C—A—S—H gels tend to

* Corresponding authors at: Physics of AmoRphous and Inorganic Solids Laboratory (PARISlab), Department of Civil and Environmental Engineering, University of California, Los Angeles, CA 90095, USA (M. Bauchy).
E-mail addresses: zw_mxx@whu.edu.cn (W. Zhou), guolijie@bgrimm.com (L. Guo), bauchy@ucla.edu (M. Bauchy).

https://doi.org/10.1016/j.jcis.2021.01.068

phase-separate. Furthermore, we demonstrate that this transition is correlated to a topological flexible-to-rigid transition within the atomic network. We reveal that the propensity for topologically-overconstrained gels to phase-separate arises from the existence of some internal stress within their atomic network, which acts as an energy penalty that drives phase separation.

1. Introduction

When reaching the saturation state, high-pH solutions comprising silicate ions gradually evolve to form hydrated silicate gels [1–3]. Such hydrated silicate gels play an important role in various applications, including cementitious materials [4,5], sol–gel glasses [3], precursors for zeolites [6], and nuclear waste glasses corrosion [7]. In particular, when exposed to water, cement (the most manufactured material in the world) tends to dissolve, thereby increasing the concentrations of Si, Al, and Ca ions in solution, and eventually resulting in the formation of calcium–silicate–hydrate (C—S—H, see all abbreviations used herein in Table 1) or calcium–aluminosilicate–hydrate (C—A—S—H) gels [8]. In turn, these hydrated gels notably affect the strength, creep resistance, and long-term durability of cement-based materials [9,10]. As such, understanding and controlling the structure of hydrated silicate gels is key to design new materials with desirable properties [11,12].

The structure of hydrated aluminosilicate gels has been extensively studied by X-ray diffraction [13], magic angle spinning nuclear magnetic resonance (MAS NMR) [14], and spectroscopy [15]. These studies have suggested that C—A—S—H gels exhibit a partially disordered atomic network [16]. At early age, such gels are mostly amorphous but still exhibit some degree of short-range order [17]. However, the degree of homogeneity/heterogeneity of the gel at the nanometer scale is more challenging to investigate. Specifically, at the nanometer scale, hydrated silicate gels can be homogeneous or phase-separated, depending on their chemical composition [18–21]. Similarly, calcium aluminosilicate systems have been noted to phase-separate—wherein the propensity for phase separation depends on stoichiometry [22]. Such phase separation can notably affect the properties of hydrated gels. Specifically, nanometric phase separation has been noted to results in an increase in the fracture toughness of hydrated gels [23–26].

From a thermodynamic viewpoint, phase separation occurs when the Gibbs free energy of the phase-separated system is lower than that of its homogenous counterpart (i.e., within the immiscibility domain) [27]. However, no clear structural origin of phase separation, should it exist, has thus far been proposed. The propensity for disordered silicates to phase separate has been suggested to be related to the existence of some preference within interpolytope bonding [28]. Specifically, disordered aluminosilicate systems typically exhibit an excess of asymmetric AlO_4–SiO_4 interpolytope bonds at the expense of AlO_4–AlO_4 linkages [29,30], which is known as the Loewenstein aluminum avoidance rule [29]. This feature is likely to hinder phase separation, since it tends to prevent the formation of Al-rich clusters within the atomic network. However, besides these considerations, it remains unclear whether the propensity for phase separation of a hydrated gel could in some ways be encoded in its atomic structure.

Here, we conduct a series of reactive molecular dynamics (MD) simulations of hydrated aluminosilicate gels with varying compositions and seek for a structural signature of the propensity for phase separation. We report the existence of a homogeneous-to-phase-separated transition, wherein Si-rich gels are homogeneous, whereas Al-rich gels are prone to phase separation. As a major outcome of this study, we demonstrate that this transition is encoded in a topological transition of the atomic network, wherein topologically-overconstrained networks tend to exhibit phase separation, whereas underconstrained networks do not. We show that, in overconstrained networks, phase separation arises from the existence of some internal stress within the atomic network, which acts as an energy penalty that drives phase separation. These results offer an atomic picture behind the propensity for phase separation in hydrated gels.

Table 1
List of abbreviations.

Abbreviations List	Definition
Al—OH	aluminol group
BO	bridging oxygen
BB	bond-bending
BS	bond-stretching
C—A—S—H	calcium–alumino–silicate–hydrate
C—S—H	calcium–silicate–hydrate
FO	free oxygen
LAMMPS	Large-scale Atomic/Molecular Massively Parallel Simulation
MAS NMR	magic angle spinning nuclear magnetic resonance
MD	molecular dynamics
NBO	nonbridging oxygen
NPT	constant number (N), pressure (P), and temperature (T)
NVT	constant number (N), volume (V), and temperature (T)
PDF	pair distribution functions
QEq	charge equilibration
Si—OH	silanol group
TCT	topological constraint theory

2. Methods

2.1. Simulated synthesis of the hydrated aluminosilicate gels

We simulate a series of hydrated aluminosilicate gels $(CaO)_{1.7}(Al_2O_3)_x(SiO_2)_{1-x}(H_2O)_{3.7+x}$ with $\times$ = 0.00, 0.02, 0.05, 0.08, 0.10, 0.12, 0.15, 0.17, 0.19, 0.22, and 0.26. The $CaO/(Al_2O_3 + SiO_2)$ molar ratio is kept fixed at 1.7, which corresponds to the average stoichiometry of the C—S—H gel forming upon the hydration of ordinary Portland cement [5,31]. Several Al_2O_3/CaO molar ratios that cover the range of experimentally-observed stoichiometries in slag-based binders [31,32] are selected to investigate the effect of the Al/Ca molar ratio. All systems comprise about 4000 atoms (see Table 2) and are simulated using the Large-scale Atomic/Molecular Massively Parallel Simulation (LAMMPS) package [33].

Starting from individual isolated $Ca(OH)_2$, $Al(OH)_3$, and $Si(OH)_4$ precursors (see below), we then simulate by reactive molecular dynamics the process of gelation—that is, the process of solidification of the system, wherein initially isolated precursors gradually react with each other to form larger clusters. To account for chemical reactions between precursors, we adopt the reactive ReaxFF force-field parametrized by Pitman et al. [34], which has been shown to offer a realistic description of the formation of hydrated silicate gels [5,35]. ReaxFF is a bond-order-based forcefield, which describes the breakage and formation of chemical bonds by calculating interatomic bond orders based on the local environment of each atom [3]. Significantly, the charge of each atom is dynamically

Table 2
Chemical composition (in terms of number of precursors) and size of the simulated $(CaO)_{1.7}(Al_2O_3)_x(SiO_2)_{1-x}(H_2O)_{3.7+x}$ gels.

x	Al/Ca ratio	$Ca(OH)_2$	$Al(OH)_3$	$Si(OH)_4$	Number of atoms
0.00	0.00	368	0	216	3784
0.02	0.03	368	10	210	3800
0.05	0.06	368	20	206	3834
0.08	0.09	368	34	199	3869
0.10	0.12	368	44	194	3894
0.12	0.14	368	52	190	3914
0.15	0.17	368	64	184	3944
0.17	0.20	368	74	180	3978
0.19	0.22	368	82	175	3989
0.22	0.26	368	96	168	4024
0.26	0.30	368	110	162	4068

assigned by employing an implemented charge equilibration (QEq) method—which is key to simulate reactivity [36]. For all these reasons, ReaxFF offers a promising pathway to simulate chemical reactions in large atomic systems with an accuracy that is comparable to *ab initio* methods at a fraction of computing cost [37,38]. Within the ReaxFF framework, the total energy of the system E_{sys} is comprised of the following ten energy terms [3,5,37]:

$$E_{sys} = E_{bond} + E_{VdWaals} + E_{Coulomb} + E_{under} + E_{over} + E_{lp} + E_{val} + E_{torsion} + E_{conj} + E_{pen} \quad (1)$$

where these energy terms are associated with, respectively, the short-range bond energy, Van der Waals energy, Coulomb potential energy, under-coordination energy, over-coordination energy, long-range electron pairs energy, valence angle energy, torsion energy, conjugation energy, and penalty energy. More details about these energy terms is available in van Duin et al. [37]. Herein, we adopt the USER-REAXC package implementation of ReaxFF, which can be found in LAMMPS [33]. The dynamics of the atoms is calculated with the velocity-Verlet integration algorithm by using a timestep of 0.25 fs.

The hydrated gels are prepared by following the methodology proposed by Côté and Cormack et al. [39], which is described in the following. First, the initial configuration of each system is generated by randomly placing some isolated $Ca(OH)_2$, $Al(OH)_3$, and $Si(OH)_4$ precursors into a cubic simulation box using the PACKMOL package [40] while avoiding any unrealistic overlap. Periodic boundary conditions are applied. The initial configuration is subjected to an energy minimization and relaxed in the canonical (*NVT*) ensemble at 300 K for 100 ps by using the Nosé-Hoover thermostat [3,41]. Subsequently, the system is relaxed at 300 K and at zero pressure in the isothermal-isobaric (*NPT*) ensemble for 500 ps [5], which is long enough to ensure convergence of both volume and energy. At this stage, no condensation reaction (i.e., formation of Si—O—Si, Al—O—Al, or Si—O—Al) between precursors is observed, as the energy barriers of such reactions are too high to be overcome within the limited timescale (i.e., a few ns) of MD simulations at 300 K. To accelerate the condensation reaction of the C—A—S—H systems, we then subject the relaxed configurations to an accelerated aging process by increasing the system temperature to 2000 K in the *NVT* ensemble for 1.25 ns. Such accelerated aging method is frequently utilized to speed up the gelation dynamics [3,5,39]. Here, the temperature of 2000 K is selected as it is large enough to overcome the condensation energy barriers, but low enough to avoid the melting of the gels [3,5]. Finally, the obtained gels are cooled from 2000 K to 300 K in the *NVT* ensemble for 100 ps, and eventually equilibrated in the *NPT* ensemble under 300 K and zero pressure for 100 ps before any further analysis. For statistical averaging purposes, all simulations are repeated 6 times. Results presented herein are averaged over these 6 repeats, while error bars are calculated based on the standard deviations of the 6 simulations.

2.2. Structural analysis

To describe the evolution of the connectivity of the C—A—S—H systems during gelation, we first compute the coordination number of each atom by counting the number of neighbors that are present in its first coordination shell. Note that the extent of the coordination shell is determined from the position of the minimum after the first peak in the partial pair distribution functions (PDF). Special attention is placed on determining the local environment of the O atoms, which is key to track the overall polymerization degree of the gels upon precipitation—since silanol (Si—OH) and aluminol (Al—OH) groups gradually transform into bridging oxygen (BO) atoms upon gelation. Based on their partial coordination numbers, O atoms are classified as bridging oxygen (BO) atoms, which are connected to two network-forming (Si or Al) atoms, and nonbridging oxygen (NBO) atoms, which are connected to only one network-forming atom [3,5].

The interpolytope connectivity is then investigated by computing the fractions of Si—O—Si, Si—O—Al, and Al—O—Al bonds in the simulated structures. To assess the level of randomness in connectivity, these fractions are compared with predictions from a random model, wherein polytopes are randomly connected to each other. Based on this model, the predicted fractions of Si—O—Si, Si—O—Al, and Al—O—Al linkages are given by:

$$f_{Si-O-Si} = \frac{(N_{Si} \times CN(Si))^2}{(N_{Si} \times CN(Si) + N_{Al} \times CN(Al))^2}$$

$$f_{Si-O-Al} = \frac{2 \times N_{Si} \times CN(Si) \times N_{Al} \times CN(Al)}{(N_{Si} \times CN(Si) + N_{Al} \times CN(Al))^2} \quad (2)$$

$$f_{Al-O-Al} = \frac{(N_{Al} \times CN(Al))^2}{(N_{Si} \times CN(Si) + N_{Al} \times CN(Al))^2}$$

where $CN(Si)$ and $CN(Al)$ are the average coordination numbers of Si and Al atoms, respectively, and N_{Si} and N_{Al} are the numbers of Si and Al atoms, respectively. Here, the average coordination number of Si or Al atoms is calculated solely based on neighboring BO atoms (i.e., NBO are excluded since they do not contribute to interpolytope linkages). Average coordination number are computed based on the population of each type of coordination species:

$$N_{Si} \times CN(Si) = 1N^{I}_{Si} + 2N^{II}_{Si} + 3N^{III}_{Si} + 4N^{IV}_{Si} \quad (3)$$

$$N_{Al} \times CN(Al) = 1N^{I}_{Al} + 2N^{II}_{Al} + 3N^{III}_{Al} + 4N^{IV}_{Al} + 5N^{V}_{Al} + 6N^{VI}_{Al} \quad (4)$$

where N^{I}_{Si}, N^{II}_{Si}, N^{III}_{Si},and N^{IV}_{Si} are the numbers of 1-, 2-, 3-, and 4-fold Si atoms, respectively, while N^{III}_{Al}, N^{IV}_{Al}, N^{V}_{Al}, and N^{VI}_{Al} are the numbers of 1-, 2-, 3-, 4-, 5-, and 6-fold Al atoms, respectively.

In addition, to better describe the degree of phase separation in C—A—S—H systems, we calculate a normalized "demixing index" [42]. First, the simulation box (with a length of about 40 Å) is split into a series of smaller cubic boxes with a length of 10 Å. We then calculate the local atomic densities of Si (ρ_{Si}) and of Al (ρ_{Al}) atoms in each of these small boxes. The demixing index (λ) is then defined as follows:

$$\frac{1}{N}\left(\frac{1}{\rho_{Si}}+\frac{1}{\rho_{Al}}\right)=\frac{1}{\lambda} \tag{5}$$

where N is a normalization coefficient that is defined so that the demixing index λ ranges from 1.0 (for a fully mixed homogeneous system, wherein the local densities of Si and Al atoms are the same in all the small boxes) to 0 (for a perfectly phase-separated system). The demixing index is then averaged over all the small boxes.

2.3. Topological constraint theory

We adopt topological constraint theory (TCT) [43–45] to characterize the network topology of the C—A—S—H gels. The state of rigidity of an atomic network is determined by the competition between the number of constraints per atom n_c and the number of degrees of freedom per atom (i.e., 3) [45]. The number of radial bond-stretching (BS) and angular bond-bending (BB) constraints created by a given atom depends in its coordination number r. In detail, the number of BS constraints is given by $r/2$ (since each constraints is shared by 2 atoms), while the number of BB constraints is given by $2r - 3$ (i.e., the number of independent angles that need to be fixed to determine the angular environment of the atom) [44]. However, although this enumeration applies to network-forming atoms (Si and Al) forming directional ionocovalent bonds with O neighbors, network-modifying atoms (Ca) create non-directional ionic bonds and, hence, are not associated with any BB constraints (since angles are not constrained). Note that isolated molecules (e.g., water molecules) are not contributing to the macroscopic rigidity of the network and, therefore, are excluded from the constraint enumeration. Here, we enumerate the constraints acting in the network of C—A—S—H based on structural inputs (e.g., coordination number r) offered by the molecular dynamics simulations. A detailed illustration of this enumeration method can be found in Bauchy *et al.* [46].

2.4. Internal stress

To quantify the stability of the atomic network, we employ the concept of "stress per atom" presented by Egami [47,48]. Strictly speaking, stress is ill-defined for single atoms and is only defined for ensembles of atoms in the thermodynamic sense [3,12]. However, a local atomic stress tensor $\sigma_i^{\alpha\beta}$ can be defined for each atom based on its contribution of each atom to the virial of the system [49]:

$$\sigma_i^{\alpha\beta}=\frac{1}{V_i}\sum_j r_{ij}^{\alpha}\cdot F_{ij}^{\beta} \tag{6}$$

where V_i is the Voronoi volume of the atom i, and r_{ij} and F_{ij} are the interatomic distance and force between atoms i and j, respectively. The superscripts α and β refer to the projections of these vectors along the Cartesian directions x, y, or z [49]. Note that, by convention, a positive local stress indicates that the atom i is locally under tension, while a negative stress denotes that the atom i is under local compression. Based on this definition, the hydrostatic stress σ_i and von Mises shear stress τ_i experienced by each atom i is described as [49]:

$$\sigma_i=\left(\sigma_i^{xx}+\sigma_i^{yy}+\sigma_i^{zz}\right)/3 \tag{7}$$

$$\tau_i=\sqrt{\left(\sigma_i^{xy}\right)^2+\left(\sigma_i^{xz}\right)^2+\left(\sigma_i^{yz}\right)^2}/3 \tag{8}$$

The terms σ_i^{xx}, σ_i^{yy}, and σ_i^{zz} refer to the three normal stress components (along the $\times$,y, and z directions, respectively), while the terms σ_i^{xy}, σ_i^{xz}, and σ_i^{yz} refer to thee three shear stress components (see Eq. (6)). Note that the presence of some local atomic-level stress does not imply the existence of a macroscopic stress, since local tensile and compressive stresses can mutually compensate each other. This atomic-level stress analysis has recently been used to describe local structural instabilities within disordered networks [50].

Furthermore, to discriminate the intrinsic stress experienced by the atoms within their local polytope from the stress contribution arising from the connectivity to the network, we repeat the atomic-level stress computation in a series of isolated molecular Q_n unit clusters for Si and Al atoms—wherein a Q_n unit represents an Si or Al atom that is connected to n BO atoms and $r - n$ NBO atoms (wherein r is the coordination number of the Si or Al atom). For example, an isolated $Si(OH)_4$ precursor is equivalent to a Q_0 unit of Si atom, while a fully-connected silica glass is made of interconnected Q_4 units. Here, each isolated cluster is created by manually placing the atoms at their designated locations [30,51]. The cluster is then placed at the center of a 50 Å large cubic box with fixed volume and no periodic boundary conditions. The initial cluster configurations are relaxed in the *NVT* ensemble at 300 K for 100 ps, cooled down to 0 K in the *NVT* ensemble for 300 ps, and finally subjected to an energy minimization. For consistency, the same ReaxFF forcefield and simulation parameters as those applied for bulk simulations are used herein. Based on this analysis, the "internal stress" is defined as the difference between the stress undergone by the network-forming species (Si and Al) in the bulk atomic network of gels and in the isolated clusters (while ensuring consistency in Q_n unit distribution). More details on the simulation of isolated clusters and atomic-level stress computation can be found in Zhao et al. [35]. To estimate the uncertainty of the internal stress values, the final configuration is relaxed at 300 K in the *NVT* ensemble for 100 ps. Ten independent configurations are subsequently extracted from this run and used for the stress calculation. The stress values are then averaged over these 10 configurations and error bars are defined based on their standard deviation.

2.5. Thermodynamic analysis

To determine how phase separation affects the thermodynamic stability of the C—A—S—H gels, we calculate their molar enthalpy before and after phase separation. This analysis is made possible by the fact that the polymerization kinetics of the gels is faster than their phase separation kinetics. In detail, we first extract the gel configurations after 0.20 ns of accelerated aging. At this time, the gels are nearly fully polymerized, but do not exhibit any sign of phase separation. The configurations are then cooled from 2000 K to 300 K in the *NVT* ensemble for 100 ps and equilibrated in the *NPT* ensemble under 300 K and zero pressure for 100 ps. The enthalpy of these polymerized, but non-phase-separated gels is then compared to their final enthalpy, i.e., after 1.25 ns of accelerated aging, which is long enough for phase separation to occur. As such, the difference between these two enthalpy quantities captures the enthalpy of phase separation.

3. Results

3.1. Simulated synthesis of the hydrated aluminosilicate gels

To study the influence of chemical composition on the precipitation mechanism and atomic structure of hydrated silicate gels, we model by reactive MD simulations a series of calcium aluminosilicate hydrate gels $(CaO)_{1.7}(Al_2O_3)_x(SiO_2)_{1-x}(H_2O)_{3.7+x}$ where x = 0%, 2%, 5%, 8%, 10%, 12%, 15%, 17%, 19%, 22%, 26% (see Methods). These compositions are selected as they range over the typical stoichiometries of C—(A—)S—H gels forming upon the hydration of ordinary Portland cement or other supplementary cementitious materials [5,31]. The simulated systems are initially comprised of isolated $Ca(OH)_2$, $Al(OH)_3$, and $Si(OH)_4$ precursors. An example atomic configuration (with Al/Ca = 0.03) after initial relaxation at 300 K is shown in Fig. 1a. At this temperature, the energy barriers associated with condensation reactions are too large to be overcome within the timescale of MD simulations—so that the precursors remain isolated from each other [3,5]. As such, we use accelerated aging at elevated temperature to simulate the gelation of these systems. Fig. 1b and c then shows the evolution of the gel structure after 0.25 ns and 1.25 ns of accelerated gelation at 2000 K, respectively. We observe that aluminate and silicate monomers gradually condensate, which manifests itself by the formation of Si—O—Si, Si—O—Al, and Al—O—Al bonds and, eventually, aluminosilicate chains and rings. Specifically, we observe that that the snapshot shown in Fig. 1c (after 1.25 ns of accelerated gelation) exhibits some additional aluminosilicate chains and rings as compared to that shown in Fig. 1b (after 0.25 ns of accelerated gelation).

We further describe the evolution of the degree of polymerization of the hydrated aluminosilicate systems upon gelation. To this end, we compute the number of bridging oxygen (BO, i.e., oxygen atoms that are connected to two Si or Al atoms) atoms per network-forming atom (i.e., Si or Al). This metric (i.e., the BO/(Si + Al) molar ratio) is initially zero when precursors are isolated from each other and would be equal to 2 in a fully connected silica glass [52]. Fig. 2a displays the evolution of the BO/(Si + Al) molar ratio as a function of time during the accelerated gelation of the hydrated gels at 2000 K. We observe that, for all the systems, the degree of polymerization gradually increases over time and eventually plateaus. This echoes previous results obtained in Al-free C—S—H gels [5]. Further, we find that the addition of Al precursors in the C—A—S—H systems tends to accelerate their polymerization kinetics.

The influence of the Al/Ca molar ratio on the connectivity of the gel at the end of the 1.25 ns accelerated aging run is illustrated in Fig. 2b. In the absence of Al atoms, our results match with previous simulations conducted on pure C—S—H [5]. We then observe that the final degree of polymerization of the gel increases with increasing Al/Ca molar ratio. This echoes the fact that the connectivity of disordered silicate phases typically increases upon the addition on Al atoms [53]. Indeed, in silicate glasses, each Ca atom creates two non-bridging oxygen (NBO, i.e., oxygen atoms that are connected to only one Si or Al atom) or one free oxygen (FO, i.e., oxygen atoms that are not connected to any Si or Al atom) to ensure charge neutrality. In contrast, Al atoms tend to reconvert such low-coordination O species into BOs by using Ca^{2+} cations to compensate the charge of AlO_4^- units [53].

3.2. Nanoscale phase separation

Next, we explore the level of homogeneity and heterogeneity in the C—A—S—H gels after accelerated gelation and a subsequent final relaxation at 300 K and zero pressure. Fig. 3a and b illustrate the final atomic configurations of two representative C—A—S—H gels with Al/Ca = 0.09 and Al/Ca = 0.30, respectively. We find that, in contrast to the fairly homogeneous character of the Si-rich gel, the Al-rich gel exhibits an obvious sign of phase separation, wherein Si and Al species are largely segregated into different regions. It should be noted that we do not observe a complete separation between Si and Al species, but, rather, a separation between "Al-free" and "Al-rich" phases. In case of Al/Ca = 0.30 (see Fig. 3b and Fig. S2), the compositions of the Al-free and Al-rich phases are $(CaO)_{1.7}(SiO_2)_{0.9}(H_2O)_{7.8}$ (33%) and $(CaO)_{1.7}(Al_2O_3)_{0.4}(SiO_2)_{0.7}(H_2O)_{2.2}$ (67%), respectively.

To further quantify the level of segregation between Si and Al, we first analyze the extent of affinity or avoidance between these two species. Fig. 3c presents the fractions of Si—O—Si, Si—O—Al, and Al—O—Al interpolytope linkages as a function of Al/Ca molar ratio. As expected, upon addition of Al atoms in the network, Si—O—Si linkages are gradually replaced by Si—O—Al and Al—O—Al bonds. The fraction of Si—O—Al linkages then reaches a maximum around Al/Ca = 0.10, while Al—O—Al bonds eventually become predominant in Al-rich gels.

To assess the existence of any avoidance between Si and Al atoms, we compare these simulated results with the predictions from a random model, that is, wherein Si and Al polytopes are randomly connected to each other (Fig. 3c). The deviation between the linkage fractions obtained from MD simulations and random models are shown in Fig. 3d, e, and f. We first observe that Si-rich gels (Al/Ca < 0.12) exhibit an excess of asymmetric Si—O—Al linkages as compared to the random model predictions (Fig. 3e) and, in turn, a deficit of symmetric Si—O—Si and Al—O—Al linkages (Fig. 3d and f). This denotes that, in this compositional regime, Si and Al polytopes exhibit some mutual affinity, while Al atoms mutually avoid each other. This echoes the "Loewenstein aluminum avoidance

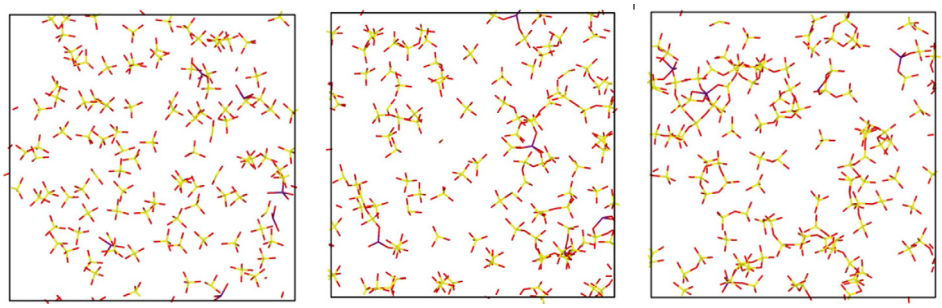

(a) t = 0.00 ns **(b)** t = 0.25 ns **(c)** t = 1.25 ns

Fig. 1. Slices showing the atomic configurations of a $CaO—Al_2O_3—SiO_2—H_2O$ (C—A—S—H) system with Al/Ca = 0.03 (a) after initial relaxation at 300 K, (b) after 0.25 ns of accelerated gelation at 2000 K, and (c) after 1.25 ns of accelerated gelation. Note that, for clarity, only Si—O and Al—O bonds are represented. Si, Al, and O atoms are colored in yellow, purple, and red, respectively. (For interpretation of the references to colour in this figure legend, the reader is referred to the web version of this article.)

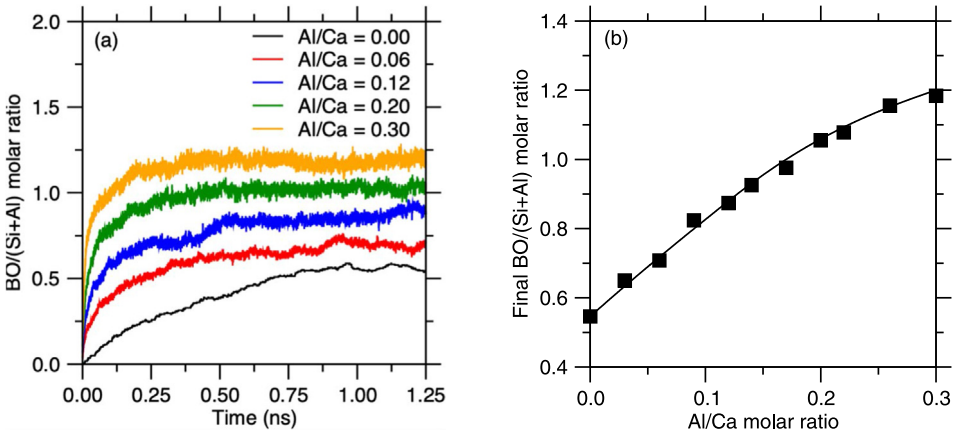

Fig. 2. (a) Number of bridging oxygen atoms per Si and Al atom (BO/(Si + Al)) in select C—A—S—H systems during accelerated aging at 2000 K. (b) Evolution of the final value of BO/(Si + Al) in C—A—S—H gels as a function of the Al/Ca molar ratio at the end of the 1.25 ns accelerated aging run. The line is to guide the eye.

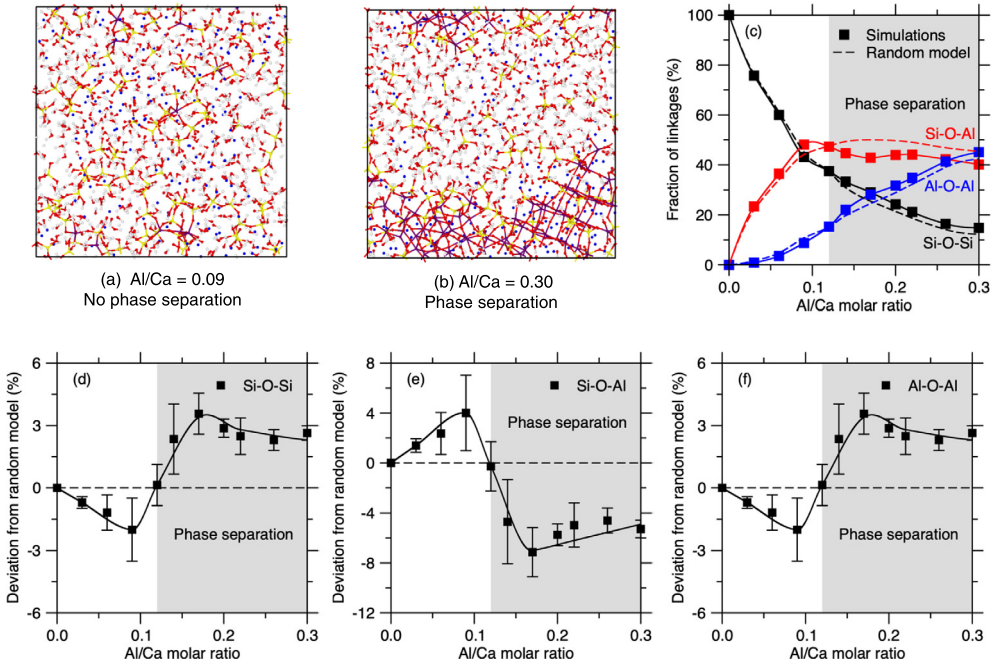

Fig. 3. Slices showing the final atomic configurations of (a) non-phase-separated and (b) phase-separated C—A—S—H gels with Al/Ca = 0.09 and Al/Ca = 0.30, respectively. Note that Ca, H, Si, Al, and O atoms are colored in blue, white, yellow, purple, and red, respectively. (c) Computed fractions of Si—O—Si, Si—O—Al, and Al—O—Al interpolytope linkages. Simulated results are compared with the predictions from a random model (see text). The differences between the fractions of Si—O—Si, Si—O—Al, and Al—O—Al bonds obtained from simulations and random model are shown in panels (d), (e), and (f), respectively. Solid lines are to guide the eye. The gray area indicates the range of compositions wherein phase separation is observed. (For interpretation of the references to colour in this figure legend, the reader is referred to the web version of this article.)

principle" observed in aluminosilicate glasses and zeolites [29,30]. Such avoidance arises from the fact that tetrahedral AlO_4 units are negatively-charged and, hence, tend to electrostatically mutually repulse each other. In contrast, we find that Al-rich gels (Al/Ca > 0.12) feature an excess of symmetric Si—O—Si and Al—O—Al linkages at the expense of asymmetric Si—O—Al bonds. This indicates that, in this domain of compositions, the Loewenstein aluminum avoidance breaks down and the Al and Si species tend avoid each other—which results in phase separation. These interpolytopes bond fractions echo the fact that the activation energy associated with the formation of Si—O—Al bonds increases upon increasing Al/Ca molar ratio (see Supplementary Material). This may explain (from a dynamic viewpoint) why such bonds eventually become unfavorable at high Al/Ca molar ratio—since the formation of symmetric Si—O—Si and Al—O—Al bonds becomes kinetically favored. Overall, these results demonstrate that C—A—S—H gels exhibit a composition-driven homogeneous-to-heterogeneous transition upon increasing Al/Ca molar ratio.

Note that Fig. 3c does not fully capture the existence of phase separation since a fraction of Si—O—Al bonds are still observed in the Al-rich phase (see Fig. 3b and Fig. S2). To better characterize the nature and extent of phase separation in this system, we calculate a normalized "demixing index" [42]. As shown in Fig. 4, we find that the average demixing index $<\lambda>$ is about 0.77 (indicative of a fairly homogeneous system) at low Al/Ca and 0.65 at high Al/Ca (indicative of a more heterogeneous system). Importantly, the average demixing index exhibits a sudden drop around Al/Ca = 0.12. These results confirm the existence of phase separation and that demixing manifests itself as a (partial) separation between Si and Al species in the gel.

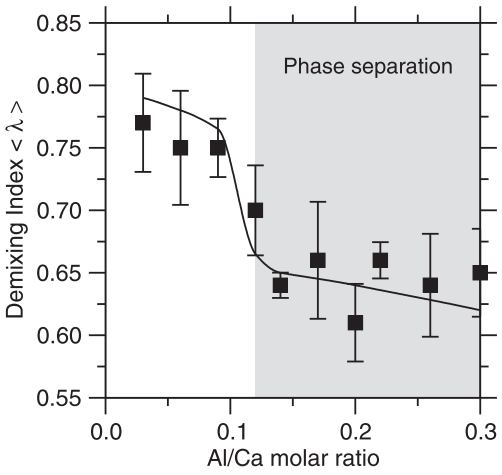

Fig. 4. Average demixing index $< \lambda >$ in simulated C—A—S—H gels as a function of the Al/Ca molar ratio—wherein small and large $< \lambda >$ values are indicative of phase-separated and homogeneous gels, respectively.

3.3. Topological origin of phase separation

Next, we explore whether the homogeneous-to-heterogeneous transition exhibited by C—A—S—H gels could in some ways be encoded in their short-range order atomic structure. First, we note that this transition is not associated with any obvious signature in coordination numbers, bond lengths, bond angles, or average ring size (see Fig. S4 in Supplementary Material). We then turn our attention to the topology of the atomic network, which has previously been shown to have a first-order influence on the properties of hydrated silicate gels [54]. To this end, we adopt the framework of topological constraint theory (TCT), which reduces the complex atomic structure of disordered phases into simpler mechanical networks, wherein some nodes (the atoms) are connected to each other by some topological constraints (the chemical bonds) [43,44,55]. This analysis is based on enumerating the topological constraints acting in the atomic network, namely, (i) the 2-body radial bond-stretching (BS) constraints that determine the interatomic distances (e.g., fixing Si—O bonds around 1.6 Å) and (ii) the 3-body angular bond-bending (BB) constraints that determine the interatomic angles (e.g., fixing O—Si—O angles around 109°). As per Maxwell's stability criterion [56], atomic networks are then classified as flexible, stressed-rigid, or isostatic when the number of constraints per atom (n_c) is lower, larger, or equal to the number of degrees of freedom per atom (i.e., 3 in three-dimensional networks), respectively [46]. As such, the number of constraints per atom n_c acts as a simple metric that captures the overall rigidity of the atomic network. More details can be found in the Methods.

Fig. 5a shows the computed number of constraints per atom n_c acting in the C—A—S—H gels as a function of the Al/Ca molar ratio. In the absence of Al, this analysis yields a number of constraints per atom $n_c = 2.82$, which matches with previous results obtained in C—S—H with Ca/Si ≈ 1.7 [46]. This confirms that, in the absence of Al, C—S—H exhibits a flexible ($n_c < 3$) atomic network. We then observe that n_c increases upon increasing Al/Ca molar ratio, in agreement with the fact that the degree of polymerization of the gel increases (see Fig. 2b). Importantly, we observe the existence of a composition-driven flexible-to-stressed-rigid transition, that is, wherein C—A—S—H gels are flexible ($n_c < 3$, underconstrained) at low Al/Ca molar ratio (Al/Ca < 0.12), stressed-rigid ($n_c > 3$, overconstrained) at high Al/Ca molar ratio (Al/Ca > 0.12), and isostatic ($n_c = 3$, optimally connected) around Al/Ca ≈ 0.12. This is notable as isostatic networks have previously been suggested to exhibit unusual mechanical and thermodynamics properties [50].

Interestingly, the flexible-to-stressed-rigid transition occurs at the same threshold composition (Al/Ca ≈ 0.12) as the homogeneous-to-heterogeneous transition, wherein flexible C—A—S—H gels remain homogeneous, whereas stressed-rigid gels tend to phase separate (see Fig. 5b). At the rigidity threshold ($n_c = 3$, Al/Ca ≈ 0.12), the interconnectivity between Si and Al polytopes matches nearly exactly the predictions from the random model (see Fig. 5b). This echoes the fact that the configurational entropy has been suggested to be maximized in isostatic glasses [57]. Overall, this surprising correlation between homogeneous-to-heterogeneous transition and network rigidity transition suggests that the propensity for phase separation is topological is nature. In the following, we explore the mechanism governing the relationship between topology and phase separation.

3.4. Internal stress drives phase separation

We now investigate the mechanistic nature of the correlation between network topology and phase separation. We propose that the propensity for stressed-rigid gels to phase separate arises from the existence of some internal stress in their atomic network. To establish this mechanism, we compute the atomic-level internal stress acting in the C—A—S—H gels following the methodology described in Zhao et al. [35]. Although, thermodynamically speaking, stress is only defined for ensembles of atoms, this approach builds on the concept of "stress per atom" introduced by Egami [47,48]. In detail, we first compute the stress per atom acting in molecular clusters made of isolated Q_n units—wherein a Q_n unit refers to a network-forming atom (Si or Al) that is surrounded by n BO atoms (e.g., glassy silica solely presents Q_4 units). We then repeat the stress per atom calculation in the bulk C—A—S—H gels. Finally, we define the "internal stress" as the difference between the stress undergone by the network-forming species (Si and Al) in the bulk atomic network of gels and in isolated clusters. This allows us to capture the stress contribution that arises from the connectivity of the atomic network [51].

Fig. 5c shows the average internal hydrostatic stress per network-forming atom (averaged over Si and Al atoms for statistical averaging purposes) with respect to the number of constraints per atom n_c. On the one hand, we note that the average internal hydrostatic stress remains fairly constant (around 38 meV/Å^3) in flexible systems ($n_c < 3$). This non-zero residual stress is a manifestation of the out-of-equilibrium nature of gels [51]. On the other hand, we observe a substantial increase in the average internal hydrostatic stress in stressed-rigid systems ($n_c > 3$), which echoes previous findings [51]. This stress arises from the fact that stressed-rigid networks exhibit an excess of constraints as compared to the number of available degrees of freedom, so that, in this overconstrained regime, all the constraints cannot be simultaneously satisfied at the same time—in the same fashion as a triangle with three fixed edge lengths cannot accommodate arbitrary angle values. The fact that the internal stress is a consequence of overconstrained nature of the atomic network is supported by the fact that the internal hydrostatic stress scales with "$n_c - 3$," which is the number of topologically-redundant constraints per atom in the network. Due to the mismatch between competing constraints within the atomic network, some constraints are slightly compressed, while others are slightly elongated—which results in the formation of some internal stress. Note that constraints exhibiting local tension and compression eventually compensate each other, so that the network remains at zero pressure at the macroscopic scale.

Besides hydrostatic stress, the rigidity transition also exhibits a signature in the internal shear stress. Fig. 5d shows the average internal von Mises shear stress per network-forming atom (averaged over Si and Al atoms) as a function of the number of con-

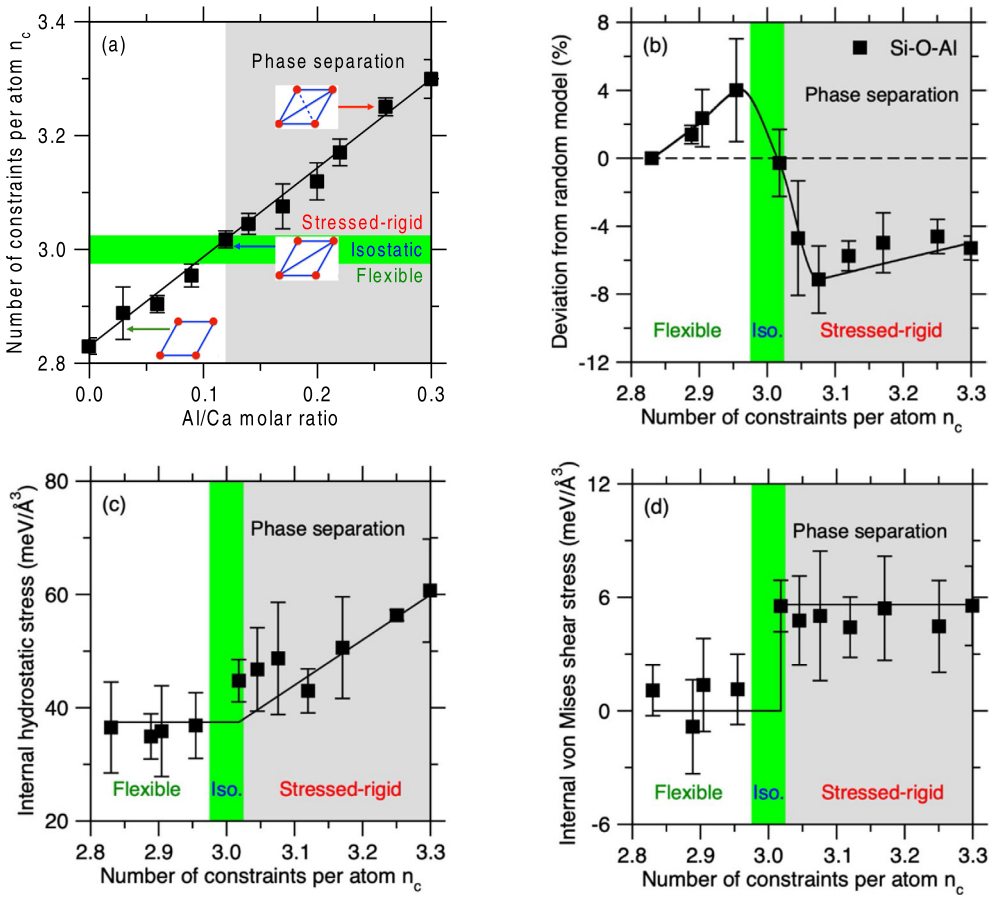

Fig. 5. (a) Computed number of constraints per atom (n_c) in C—A—S—H gels as a function of the Al/Ca molar ratio. (b) Difference between the fraction of Si—O—Al interpolytope linkages obtained from simulations and random model as a function of n_c. Internal (c) hydrostatic stress (d) and von Mises shear stress averaged over all the network-forming (Si and Al) atoms as a function of n_c. The solid lines are to guide the eye. The green area indicates the isostatic compositional domain that is at the vicinity of the rigidity transition ($n_c \approx 3$), while the gray area denotes the range of stressed-rigid compositions ($n_c > 3$) wherein phase separation is observed. (For interpretation of the references to colour in this figure legend, the reader is referred to the web version of this article.)

straints per atom n_c. We note that network-forming atoms do not undergo any von Mises shear stress in the flexible regime ($n_c < 3$). We then observe a sudden discontinuity in shear stress at the rigidity transition, wherein stressed-rigid systems exhibit a non-zero internal von Mises shear stress. In this overconstrained regime ($n_c > 3$), the internal von Mises shear stress remains fairly constant (around 6 meV/Å^3). The fact that, in contrast to the hydrostatic stress, the internal shear stress does not linearly increase with the number of redundant constraints may be a consequence of the fact that atomic structures that are subjected to a large shear stress eventually exhibit some local yielding, so that the shear stress cannot accumulate any further. The magnitude of internal shear stress is notably smaller than that of the hydrostatic stress.

Overall, these results establish that the propensity for C—A—S—H gels to phase separate is correlated to the onset of internal hydrostatic and shear stress in the atomic network, which, in turn, is a consequence of the overconstrained topological nature of such Al-rich gels. This suggests that the propensity for phase separation is topological in nature.

4. Discussion

Next, we discuss the physical nature of the relationship between network topology, internal stress, and phase separation. The link between stress and phase separation can be understood based on the following atomic picture. Flexible systems exhibit an excess of degrees of freedoms, so that all the radial and angular constraints created by the chemical bonds can be fully accommodated. In this regime, there is no atomic driving force for phase separation. As the connectivity of the system increases (i.e., upon addition of Al atoms here), topological constraints eventually exhaust available degrees of freedom and become mutually redundant (e.g., if all edge lengths and angles are fixed, a triangle exhibit 3 redundant constraints). In this overcoordinated regime, excess radial and angular constraints start to compete against each other, which results in the formation of internal stress.

Note that, even in the overcoordinated regime, no stress would form if all these redundant constraints were perfect compatible with each other like in an ordered crystalline structure. However, such mutual compatibility is not possible in homogeneous disordered C—A—S—H gels since Si and Al polytopes exhibit different sizes and local angular environments. In this regime, the internal stress due to redundant constraints acts as an elastic energy penalty, which renders unstable the atomic network. Starting from this situation, it becomes clear that phase separation then acts as a mechanism that enables the atomic network to release this energy penalty. Indeed, by phase separating, the network eventually forms distinct Al-free and Al-rich domains. Although this does not reduce the overall number of constraints, phase separation makes it possible for the redundant constraints to become compatible with each other—since Al polytopes now become solely connected to similar, compatible polytopes, i.e., with consistent size and angular environment.

Although the facts that (i) Al-rich gels tend to phase separate and (ii) phase separation results in the formation of a stable Al-rich phase seem to be self-contradicting, this apparent contradiction can be resolved based on the following. Our main point is that phase separation results from the existence of some internal stress within the network, while, in turn, phase separation allows the network to release this stress. Indeed, before phase separation, overconstrained Al-rich gels exhibit an excess of topological constraints as compared to the number of degrees of freedom—so that all the constraints cannot be satisfied at the same time. This results in the formation of internal stress, which, in turn, induces phase separation. However, although the Al-rich phase forming after phase separation is also overconstrained, it should be emphasized that an excess of constraints does not necessarily induce phase separation. Indeed, most crystals (e.g., quartz) are overconstrained [58] and, yet, do not phase separate since their organized structure makes it possible for the constraints to match each other. As another example, a triangle comprising 6 constraints (3 edges and 3 angles) can be topologically stable—provided that the value of the angles is compatible with that of the edges. In other words, an excess of constraints will only result in internal stress if these constraints cannot be mutually compatible. Here, the abundance of Al atoms in the Al-rich phase forming after phase separation also makes it possible for the constraints created by these atoms to be mutually compatible—since Al atoms are connected to other Al atoms, which exhibit the same local environment. In fact, this compatibility between constraints becomes apparent when observing the structure of the Al-rich phase (see Fig. 3b and Fig. S2), which exhibits a large degree of angular ordering and a fairly periodic structure. This level of ordering explains how this newly-formed Al-rich phase can be simultaneously overconstrained and topologically stable.

To establish the idea of phase separation being a mechanism aiming to release the elastic energy associated with the internal in stressed-rigid systems, we track the evolution of the enthalpy of the C—A—S—H gels during accelerated aging. Specifically, Fig. 6 shows the difference in enthalpy before and after phase separation as a function of the number of constraints per atom n_c. This analysis is made possible by the fact that the initial polymerization (i.e., increase in connectivity) of the gels is fairly fast (see Fig. 2a),

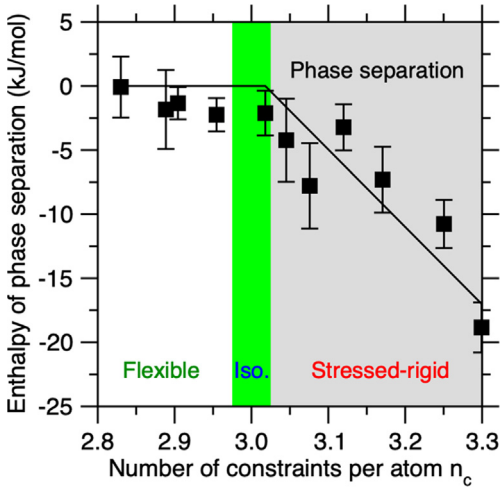

Fig. 6. Enthalpy difference before and after phase separation in C—A—S—H as a function of the number of constraints per atom n_c. The solid line is to guide the eye. The green area indicates the isostatic compositional domain that is at the vicinity of the rigidity transition ($n_c \approx 3$), while the gray area denotes the range of stressed-rigid compositions ($n_c > 3$) wherein phase separation is observed. (For interpretation of the references to colour in this figure legend, the reader is referred to the web version of this article.)

while phase separation is a slower phenomenon. This allows us to compute the effect of phase separation on enthalpy at fixed connectivity (i.e., fixed n_c). As shown in Fig. 6, we find that flexible systems ($n_c < 3$) do not exhibit any notable variation in enthalpy, in agreement with the fact that such gels do not phase separate. In contrast, we observe that stressed-rigid systems ($n_c > 3$) present a notable decrease in enthalpy. This indicates that, in this regime, phase separation allows the gels to reach a lower energy state, that is, to become more stable. Importantly, we find that the decrease in enthalpy exhibits a fair scaling with "$n_c - 3$", i.e., the number of redundant constraints per atom in the network. This confirms that phase separation acts as an energy dissipation mechanism that allows the network to release the elastic energy penalty associated with the onset of internal stress in stressed-rigid networks.

5. Conclusions

Altogether, this study explores the origin and mechanism of nanoscale phase separation in hydrated colloidal gels. Our molecular dynamics simulations offer a realistic description of the time-dependent gelation of C—A—S—H gels with various compositions. By comparing simulated data with the predictions from a random model, we find the existence of a homogeneous-to-phase-separated transition—wherein Si-rich C—A—S—H gels (Al/Ca < 0.12) are homogeneous, whereas Al-rich C—A—S—H gels (Al/Ca > 0.12) tend to phase-separate. The existence (or absence) of phase separation is encoded in the propensity (or not) for the gel to avoid Al—O—Al bonds—as dictated by the "Loewenstein aluminum avoidance principle" [29,30]. As a major outcome of this study, we demonstrate that this transition is correlated to a topological flexible-to-rigid transition within the atomic network—wherein topologically-underconstrained (flexible) gels tend to remain homogeneous, whereas topologically-overconstrained (stressed-rigid) gels tend to phase separate. Finally, by adopting the concept of "stress per atom," we reveal that the propensity for overconstrained gels to phase-separate arises from the existence of some internal stress with-in their atomic network, which acts as an energy penalty that drives phase separation.

Overall, these results suggest that phase separation is a direct consequence of network topology and is essentially a mechanism for stressed-rigid disordered networks to release the internal stress that results from mutually dependent topological constraints. It should be noted that, even when it is thermodynamically favorable, phase separation cannot proceed if its kinetics is too slow, that is, if it is associated with large energy barriers. In that regard, the elastic energy penalty resulting from redundant constraints in stressed-rigid networks can effectively reduce this energy barrier by destabilizing the atomic network. Altogether, these results reveal an unexpected relationship between atomic topology, thermodynamics, and propensity for phase separation.

This linkage between network topology and phase separation that is presented herein is supported by the fact that stressed-rigid sodium silicate glasses (with <20% molar fraction of Na_2O) [59] also tend to phase separate [60,61]. This idea also echoes the fact that stressed-rigid glass-forming melts typically exhibit a high propensity for crystallization and, thereby, tend to present low glass-forming ability [55]. Indeed, besides phase separation, crystallization (when kinetically allowed) can also be another mechanism enabling the atomic network to release such internal stress.

Based on our findings, we envision that the topological approach developed herein could offer a generic framework to decipher how the propensity for disordered phases to phase separate or crystalize is encoded in their atomic structure. Assessing the generality of this result would require extending this analysis

to a broader range of disordered systems. Although it is challenging to experimentally access the time-dependent structure of phase-separating systems, it has been suggested that the internal stress that is at play in overconstrained networks can be tracked by Raman scattering [62]. Such analyses would be key to validate the mechanism that is presented herein. Finally, we envision that the careful control of phase separation in hydrated gels could open a new degree of freedom (besides composition and packing density) to design novel gels with unusual properties.

CRediT authorship contribution statement

Cheng Zhao: Conceptualization, Data curation, Formal analysis, Writing - original draft, Writing - review & editing. **Wei Zhou:** Investigation, Writing - review & editing, Supervision. **Qi Zhou:** Data curation, Formal analysis. **Zhe Wang:** Data curation, Software, Visualization. **Gaurav Sant:** Investigation, Writing - review & editing. **Lijie Guo:** Funding acquisition, Writing - review & editing, Project administration. **Mathieu Bauchy:** Methodology, Formal analysis, Writing - review & editing, Resources, Supervision.

Declaration of Competing Interest

The authors declare that they have no known competing financial interests or personal relationships that could have appeared to influence the work reported in this paper.

Acknowledgements

The authors acknowledge some financial support provided by the National Key Research and Development Program of China under Grant No. 2016YFC0401907, the National Natural Science Foundation of China under Grant No. 51879206, the International Graduate Student Exchange Program of Wuhan University, and the China Scholarship Council (Grant No. 201906270098). Part of this work was also supported by the National Science Foundation under Grants No. CMMI-1762292, DMREF-1922167, and DMR-1944510, the Department of Energy's Nuclear Energy University Program (DOE-NEUP: DE-NE18-15020), as well as the International Cooperation on Scientific and Technological Innovation Programs of BGRIMM under Grant No. 2017YFE0107000.

Data availability

The data that support the findings of this study are available from the corresponding authors upon reasonable request.

Appendix A. Supplementary material

Supplementary data to this article can be found online at https://doi.org/10.1016/j.jcis.2021.01.068.

References

[1] B.C. Bunker, Molecular mechanisms for corrosion of silica and silicate glasses, J. Non-Cryst. Solids. 179 (1994) 300–308, https://doi.org/10.1016/0022-3093(94)90708-0.
[2] G. Kaur, G. Pickrell, N. Sriranganathan, V. Kumar, D. Homa, Review and the state of the art: Sol–gel and melt quenched bioactive glasses for tissue engineering, J. Biomed. Mater. Res. B Appl. Biomater. 104 (2016) 1248–1275, https://doi.org/10.1002/jbm.b.33443.
[3] T. Du, H. Li, G. Sant, M. Bauchy, New insights into the sol–gel condensation of silica by reactive molecular dynamics simulations, J. Chem. Phys. 148 (2018) 234504, https://doi.org/10.1063/1.5027583.
[4] H.F.W. Taylor, Proposed structure for calcium silicate hydrate gel, J. Am. Ceram. Soc. 69 (1986) 464–467, https://doi.org/10.1111/j.1151-2916.1986.tb07446.x.
[5] T. Du, H. Li, Q. Zhou, Z. Wang, G. Sant, J.V. Ryan, M. Bauchy, Chemical composition of calcium-silicate-hydrate gels: Competition between kinetics and thermodynamics, Phys. Rev. Mater. 3 (2019) 065603, https://doi.org/10.1103/PhysRevMaterials.3.065603.
[6] P. Phiriyawirut, R. Magaraphan, A.M. Jamieson, S. Wongkasemjit, MFI zeolite synthesis directly from silatrane via sol–gel process and microwave technique, Mater. Sci. Eng. A. 361 (2003) 147–154, https://doi.org/10.1016/S0921-5093(03)00509-4.
[7] J.D. Vienna, J.V. Ryan, S. Gin, Y. Inagaki, Current understanding and remaining challenges in modeling long-term degradation of borosilicate nuclear waste glasses, Int. J. Appl. Glass Sci. 4 (2013) 283–294, https://doi.org/10.1111/ijag.12050.
[8] H.M. Dyson, I.G. Richardson, A.R. Brough, A Combined 29Si MAS NMR and selective dissolution technique for the quantitative evaluation of hydrated blast furnace slag cement blends, J. Am. Ceram. Soc. 90 (2007) 598–602, https://doi.org/10.1111/j.1551-2916.2006.01431.x.
[9] S.-D. Wang, K.L. Scrivener, Hydration products of alkali activated slag cement, Cem. Concr. Res. 25 (1995) 561–571, https://doi.org/10.1016/0008-8846(95)00045-E.
[10] K. Ioannidou, M. Kanduč, L. Li, D. Frenkel, J. Dobnikar, E. Del Gado, The crucial effect of early-stage gelation on the mechanical properties of cement hydrates, Nat. Commun. 7 (2016) 12106, https://doi.org/10.1038/ncomms12106.
[11] R. Hellmann, S. Cotte, E. Cadel, S. Malladi, L.S. Karlsson, S. Lozano-Perez, M. Cabié, A. Seyeux, Nanometre-scale evidence for interfacial dissolution–reprecipitation control of silicate glass corrosion, Nat. Mater. 14 (2015) 307–311, https://doi.org/10.1038/nmat4172.
[12] T. Du, H. Li, Q. Zhou, Z. Wang, G. Sant, J.V. Ryan, M. Bauchy, Atomistic origin of the passivation effect in hydrated silicate glasses, Npj Mater. Degrad. 3 (2019) 1–7, https://doi.org/10.1038/s41529-019-0070-9.
[13] J.L. Provis, A. Palomo, C. Shi, Advances in understanding alkali-activated materials, Cem. Concr. Res. 78 (2015) 110–125, https://doi.org/10.1016/j.cemconres.2015.04.013.
[14] I.G. Richardson, J. Skibsted, L. Black, R.J. Kirkpatrick, Characterisation of cement hydrate phases by TEM, NMR and Raman spectroscopy, Adv. Cem. Res. 22 (2010) 233–248, https://doi.org/10.1680/adcr.2010.22.4.233.
[15] J. Yarwood, R. Douthwaite, S. Duckett, Spectroscopic Properties of Inorganic and Organometallic Compounds, vol. 40, Royal Society of Chemistry, 2009.
[16] C. Meral, C.J. Benmore, P.J.M. Monteiro, The study of disorder and nanocrystallinity in C-S–H, supplementary cementitious materials and geopolymers using pair distribution function analysis, Cem. Concr. Res. 41 (2011) 696–710, https://doi.org/10.1016/j.cemconres.2011.03.027.
[17] G.N. Greaves, S. Sen, Inorganic glasses, glass-forming liquids and amorphizing solids, Adv. Phys. 56 (2007) 1–166, https://doi.org/10.1080/00018730601147426.
[18] M. Tomozawa, S. Capella, Microstructure in hydrated silicate glasses, J. Am. Ceram. Soc. 66 (1983), https://doi.org/10.1111/j.1151-2916.1983.tb10000.x.
[19] B.C. Bunker, T.J. Headley, S.C. Douglas, Gel structures in leached alkali silicate glass, MRS Online Proc. Libr. Arch. 32 (1984), https://doi.org/10.1557/PROC-32-41.
[20] S. Börjesson, A. Emrén, C. Ekberg, A thermodynamic model for the calcium silicate hydrate gel, modelled as a non-ideal binary solid solution, Cem. Concr. Res. 27 (1997) 1649–1657, https://doi.org/10.1016/S0008-8846(97)00149-X.
[21] Y. Li, H. Sun, X. Liu, Z. Cui, Effect of phase separation structure on cementitious reactivity of blast furnace slag, Sci. China Ser. E Technol. Sci. 52 (2009) 2695–2699, https://doi.org/10.1007/s11431-008-0239-x.
[22] L. Martel, M. Allix, F. Millot, V. Sarou-Kanian, E. Véron, S. Ory, D. Massiot, M. Deschamps, Controlling the size of nanodomains in calcium aluminosilicate glasses, J. Phys. Chem. C. 115 (2011) 18935–18945, https://doi.org/10.1021/jp200824m.
[23] P.F. James, Liquid-phase separation in glass-forming systems, J. Mater. Sci. 10 (1975) 1802–1825, https://doi.org/10.1007/BF00554944.
[24] N. Kreidl, Phase separation in glasses, J. Non-Cryst. Solids. 129 (1991) 1–11, https://doi.org/10.1016/0022-3093(91)90074-G.
[25] K.V. Tian, B. Yang, Y. Yue, D.T. Bowron, J. Mayers, R.S. Donnan, C. Dobó-Nagy, J. W. Nicholson, D.-C. Fang, A.L. Greer, G.A. Chass, G.N. Greaves, Atomic and vibrational origins of mechanical toughness in bioactive cement during setting, Nat. Commun. 6 (2015) 8631, https://doi.org/10.1038/ncomms9631.
[26] H. Guo, N. Sanson, D. Hourdet, A. Marcellan, Thermoresponsive toughening with crack bifurcation in phase-separated hydrogels under isochoric conditions, Adv. Mater. 28 (2016) 5857–5864, https://doi.org/10.1002/adma.201600514.
[27] D. Blankschtein, G.M. Thurston, G.B. Benedek, Phenomenological theory of equilibrium thermodynamic properties and phase separation of micellar solutions, J. Chem. Phys. 85 (1986) 7268–7288, https://doi.org/10.1063/1.451365.
[28] L.-S. Du, J.F. Stebbins, Solid-state NMR study of metastable immiscibility in alkali borosilicate glasses, J. Non-Cryst. Solids. 315 (2003) 239–255, https://doi.org/10.1016/S0022-3093(02)01604-6.
[29] W. Loewenstein, The distribution of aluminum in the tetrahedra of silicates and aluminates, Am. Mineral. 39 (1954) 92–96.
[30] M. Bauchy, Structural, vibrational, and elastic properties of a calcium aluminosilicate glass from molecular dynamics simulations: The role of the potential, J. Chem. Phys. 141 (2014) 024507, https://doi.org/10.1063/1.4886421.
[31] I.G. Richardson, G.W. Groves, Microstructure and microanalysis of hardened ordinary Portland cement pastes, J. Mater. Sci. 28 (1993) 265–277, https://doi.org/10.1007/BF00349061.

[32] B. Lothenbach, K. Scrivener, R.D. Hooton, Supplementary cementitious materials, Cem. Concr. Res. 41 (2011) 1244–1256, https://doi.org/10.1016/j.cemconres.2010.12.001.
[33] S. Plimpton, Fast parallel algorithms for short-range molecular dynamics, J. Comput. Phys. 117 (1995) 1–19, https://doi.org/10.1006/jcph.1995.1039.
[34] M.C. Pitman, A.C.T. van Duin, Dynamics of confined reactive water in smectite clay-zeolite composites, J. Am. Chem. Soc. 134 (2012) 3042–3053, https://doi.org/10.1021/ja208894m.
[35] C. Zhao, W. Zhou, Q. Zhou, Y. Zhang, H. Liu, G. Sant, X. Liu, L. Guo, M. Bauchy, Precipitation of calcium–alumino–silicate–hydrate gels: The role of the internal stress, J. Chem. Phys. CLMD2020 (2020) 014501, https://doi.org/10.1063/5.0010476@jcp.2020.CLMD2020.issue-1.
[36] E. Demiralp, T. Çağin, W.A. Goddard, Morse stretch potential charge equilibrium force field for ceramics: application to the quartz-stishovite phase transition and to silica glass, Phys. Rev. Lett. 82 (1999) 1708–1711, https://doi.org/10.1103/PhysRevLett.82.1708.
[37] A.C.T. van Duin, S. Dasgupta, F. Lorant, W.A. Goddard, ReaxFF: A reactive force field for hydrocarbons, J. Phys. Chem. A. 105 (2001) 9396–9409, https://doi.org/10.1021/jp004368u.
[38] C. Mischler, W. Kob, K. Binder, Classical and ab-initio molecular dynamic simulation of an amorphous silica surface, Comput. Phys. Commun. 147 (2002) 222–225, https://doi.org/10.1016/S0010-4655(02)00250-3.
[39] A.S. Côté, A.N. Cormack, A. Tilocca, Influence of calcium on the initial stages of the sol-gel synthesis of bioactive glasses, J. Phys. Chem. B. 120 (2016) 11773–11780, https://doi.org/10.1021/acs.jpcb.6b09881.
[40] L. Martínez, R. Andrade, E.G. Birgin, J.M. Martínez, PACKMOL: A package for building initial configurations for molecular dynamics simulations, J. Comput. Chem. 30 (2009) 2157–2164, https://doi.org/10.1002/jcc.21224.
[41] W.G. Hoover, Canonical dynamics: Equilibrium phase-space distributions, Phys. Rev. A. 31 (1985) 1695–1697, https://doi.org/10.1103/PhysRevA.31.1695.
[42] N. Sieffert, G. Wipff, The [BMI][Tf2N] ionic liquid/water Binary system: A molecular dynamics study of phase separation and of the liquid–liquid interface, J. Phys. Chem. B. 110 (2006) 13076–13085, https://doi.org/10.1021/jp061849q.
[43] J.C. Phillips, Topology of covalent non-crystalline solids I: Short-range order in chalcogenide alloys, J. Non-Cryst. Solids. 34 (1979) 153–181, https://doi.org/10.1016/0022-3093(79)90033-4.
[44] J.C. Mauro, Topological constraint theory of glass, Am. Ceram. Soc. Bull. 90 (2011) 31–37.
[45] J.C. Phillips, Topology of covalent non-crystalline solids II: Medium-range order in chalcogenide alloys and A Si(Ge), J. Non-Cryst. Solids. 43 (1981) 37–77, https://doi.org/10.1016/0022-3093(81)90172-1.
[46] M. Bauchy, M.J. Abdolhosseini Qomi, C. Bichara, F.-J. Ulm, R.J.-M. Pellenq, Nanoscale structure of cement: viewpoint of rigidity theory, J. Phys. Chem. C. 118 (2014) 12485–12493, https://doi.org/10.1021/jp502550z.
[47] V. Vitek, T. Egami, Atomic level stresses in solids and liquids, Phys. Status Solidi B. 144 (1987) 145–156, https://doi.org/10.1002/pssb.2221440113.
[48] T. Egami, Atomic level stresses, Prog. Mater. Sci. 56 (2011) 637–653, https://doi.org/10.1016/j.pmatsci.2011.01.004.
[49] W. Song, X. Li, B. Wang, N.M. Anoop Krishnan, S. Goyal, M.M. Smedskjaer, J.C. Mauro, C.G. Hoover, M. Bauchy, Atomic picture of structural relaxation in silicate glasses, Appl. Phys. Lett. 114 (2019) 233703, https://doi.org/10.1063/1.5095529.
[50] Q. Zhou, M. Wang, L. Guo, P. Boolchand, M. Bauchy, Intermediate phase in calcium–silicate–hydrates: mechanical, structural, rigidity, and stress signatures, Front. Mater. 6 (2019), https://doi.org/10.3389/fmats.2019.00157.
[51] X. Li, W. Song, M.M. Smedskjaer, J.C. Mauro, M. Bauchy, Quantifying the internal stress in over-constrained glasses by molecular dynamics simulations, J. Non-Cryst. Solids X. 1 (2019) 100013, https://doi.org/10.1016/j.nocx.2019.100013.
[52] Z. Strnad, Role of the glass phase in bioactive glass-ceramics, Biomaterials 13 (1992) 317–321, https://doi.org/10.1016/0142-9612(92)90056-T.
[53] A.K. Varshneya, Fundamentals of Inorganic Glasses, Elsevier, 2013.
[54] H. Liu, T. Du, N.M.A. Krishnan, H. Li, M. Bauchy, Topological optimization of cementitious binders: Advances and challenges, Cem. Concr. Compos. 101 (2019) 5–14, https://doi.org/10.1016/j.cemconcomp.2018.08.002.
[55] M. Bauchy, Deciphering the atomic genome of glasses by topological constraint theory and molecular dynamics: A review, Comput. Mater. Sci. 159 (2019) 95–102, https://doi.org/10.1016/j.commatsci.2018.12.004.
[56] J. Clerk Maxwell F.R.S. L. On the calculation of the equilibrium and stiffness of frames, Lond. Edinb. Dublin Philos. Mag. J. Sci. 27 (1864) 294–299. https://doi.org/10.1080/14786446408643668.
[57] S. Chakravarty, R. Chbeir, P. Chen, M. Micoulaut, P. Boolchand, Correlating melt dynamics and configurational entropy change with topological phases of glasses and the crucial role of melt/glass homogenizationAs_xS_{100-x}, Front. Mater. 6 (2019), https://doi.org/10.3389/fmats.2019.00166.
[58] M. Bauchy, Topological constraint theory and rigidity of glasses, ArXiv200504603 Cond-Mat. (2019), https://doi.org/10.1201/9780367333003.
[59] Y. Vaills, T. Qu, M. Micoulaut, F. Chaimbault, P. Boolchand, Direct evidence of rigidity loss and self-organization in silicate glasses, J. Phys. Condens. Matter. 17 (2005) 4889–4896, https://doi.org/10.1088/0953-8984/17/32/003.
[60] B.R. Wheaton, A.G. Clare, Evaluation of phase separation in glasses with the use of atomic force microscopy, J. Non-Cryst. Solids. 353 (2007) 4767–4778, https://doi.org/10.1016/j.jnoncrysol.2007.06.073.
[61] A. Hodroj, P. Simon, P. Florian, M.-H. Chopinet, Y. Vaills, Phase separation and spatial morphology in sodium silicate glasses by AFM, light scattering and NMR, J. Am. Ceram. Soc. 96 (2013) 2454–2460, https://doi.org/10.1111/jace.12459.
[62] F. Wang, S. Mamedov, P. Boolchand, B. Goodman, M. Chandrasekhar, Pressure Raman effects and internal stress in network glasses, Phys. Rev. B. 71 (2005) 174201, https://doi.org/10.1103/PhysRevB.71.174201.